

Nonlinear dynamics of a vertical pendulum driven by magnetic field provided by two coils magnets: analytical, numerical and experimental studies

B. Nana^{a*}, K. Polczyński^b, P. Wofo^c and J. Awrejcewicz^b.

Received: date / Accepted: date

Abstract In the present work, we analyzed theoretically and experimentally the nonlinear dynamics of a magnetic pendulum excited through the interactions of a strong neodymium magnet and two coils placed symmetrically around the zero angular position. The forces between the magnet and coils and generated torques acting on the pendulum are derived using the magnetic charges interaction model and an experimentally fitted model. System equilibrium points are obtained, and their stability is investigated. It is found that when the currents in two coils are negative, the shape of the mechanical potential is bistable. The bistable potential might be symmetric if the currents have the same values and asymmetric when they are different. Asymmetric bistable potential is observed when coil currents have different signs. However, in the case of positive coil currents, a symmetric tristable potential is detected when the currents are the same, and an asymmetric tristable potential takes place when the positive currents have different values. Considering the sinusoidal coil current signals, analytical calculations using the harmonic balance method and numerical simulations are carried out for this electric-magneto-mechanical system. The obtained results are shown in terms of frequency-response diagrams, displacement time series, and phase portraits. The two-parameter bifurcation diagrams are plotted showing the different dynamical behaviors considering the current amplitudes and frequency as the control parameters. Amplitude jumps, hysteresis, and multistability are also observed. Some phase portraits and the coexistence of attractors are obtained numerically and confirmed experimentally. A good agreement between the numerical simulation and experimental measurement is achieved.

^{a*} Department of Physics, Higher Teacher Training College, University of Bamenda, PO Box 39 Bamenda, Cameroon. E-mail: na1bo@yahoo.fr

^b Department of Automation, Biomechanics, and Mechatronics, Lodz University of Technology, 1/15 Stefanowskiego Str., 90-537 Lodz, Poland

^c Laboratory of Modelling and Simulation in Engineering, Biomimetics and Prototypes, Faculty of Science, University of Yaounde I, PO Box 812 Yaounde, Cameroon.

Keywords Magnetic pendulum · magnetic field · multistability · bifurcation analysis · tristable potential

1 Introduction

In recent years, several theoretical and experimental studies demonstrating chaotic motion in pendulum systems have been published. This has motivated intense research that has led to the discovery of many novel features of pendulum systems [1–9]. Mechanical systems including the pendulum arise in many practical applications in mechanical/mechatronic engineering such as machines and mechanisms, control and automation devices, space exploration machines, sensors, robots, and servos construction, as well as several MEMS and NEMS devices [10–22].

Recently, there has been increasing interest in the design and implementation of magnetic pendulums [23–31]. A magnetic pendulum is considered as a mechanical system in which the upper end is fixed to a rotational axis, and a permanent magnet or ferromagnetic bob is installed on its other end. The unit composed of a pendulum-magnet moves under the action of another permanent magnet or electromagnet located close to its lower end. In general, the vertical magnetic pendulum is affected by two potential energies; namely, the gravitational potential energy, and the magnetic potential energy.

An interesting system based on a magnetic pendulum for positioning offshore wind turbines during their installation has been presented by Atzampou et al. [32]. The contactless motion compensation technique has been validated numerically and experimentally. The obtained results have illuminated the path for further potential to increase the efficiency of offshore wind installations.

Pilipchuk et al. [33] have studied a system composed of two weakly coupled magnetic pendulums. The authors have developed algorithms for controlling an energy transfer between pendulums using a proper magnetic field generated by coils placed under the pendulums. Numerical, analytical, and experimental investigations have been performed which have proved that analyzed transfer energy control algorithms work properly and can be used in energy harvesting and vibration-damping systems.

Magnetic pendulum arrays were recently employed as an antenna for efficient transmission in ultra-low frequencies (ULF) [34,35]. The antenna was composed of 28 cylindrical magnets. Assuming that magnets behave like magnetic pendulums, the authors analyzed their vibrations and efficiency in generating electromagnetic waves in the ultra-low frequency range. As a result, it turned out that the efficiency of this type of antenna is 7 dB higher than that of an ordinary electric antenna.

Inspired by the results of papers [28,36] regarding a magnetic pendulum subjected to the action of one coil at its base and those reported in Ref. [29] for horizontal magnetic pendulum subjected to the action of fixed magnets placed symmetrically to the reference horizontal direction, this work is aimed to analyze the dynamical behavior of a magnetic pendulum driven by two coils. **The permanent magnet is positioned at the lower end of the pendulum and the axis of the coils are symmetric with respect to the pendulum vertical position. Compared to the other works mentioned previously, this system presents a bistable or tristable potential depending on the parameters. Hence, the objective of this work is to analyze the effects of such potential on the dynamical behavior of the system. The analysis employs mathematical, numerical, and experimental methods.** In this work, magnet and coils are considered as magnetic

charges and we have used an equivalent Coulomb law to derive the formulas of the magnetic torques governing coil-magnet pair interaction [25, 26, 37]. This magnetic charge interaction model has been used recently by the authors of reference [25] and excellent agreement was found between their theoretical and experimental results.

The paper is structured in the following order. The physical description and the mathematical model of the system are presented in Section 2. The equilibrium points and their stability as well as the shapes of the system and the shapes of the corresponding potential are analyzed in Section 3 where the solenoids are powered with constant current sources. In Section 4, the current is taken to be a sinusoidal one. We find mathematically the frequency response of the system invoking the harmonic balance method. Then, we apply the numerical simulation to complement the mathematical results and plot the numerous bifurcation diagrams exhibiting novel dynamic phenomena. In Section 5, comparisons between our simulations and experimental results are presented. Our conclusions are contained in the final section and present concluding remarks of our research.

2 Physical and mathematical models

2.1 Physical model

A schematic representation of the magnetic pendulum driven by two magnetic forces is shown in Figure 1, where θ is the angular deviation.

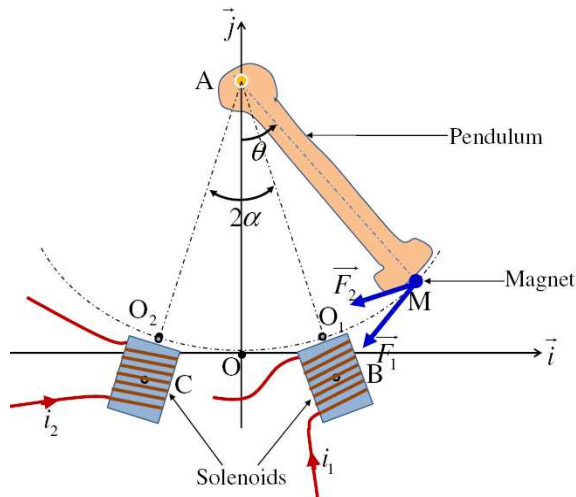


Fig. 1 Pendulum-magnet embedded into a variable magnetic field invoked by two current-carrying solenoids.

It is assumed that the pendulum motion is confined to the (x, y) -plane and that the pivot is at the origin of the coordinate system. The potential energy of the pendulum is caused by the gravity field. The level of zero potential is considered to be the xz plane of the chosen coordinate system. As indicated in the figure, a strong neodymium

magnet is joined to the free end of the pendulum while the upper end of the pendulum is fixed to a horizontal rotational axis. Two current-carrying solenoids are placed under the pendulum arm, and the axis of the first solenoid located at point B is attributed to an angle α with the vertical axis, namely the y -axis. Similarly, the axis of the second solenoid located at point C makes an angle $-\alpha$ with the vertical axis. Points B and C are the centers of the first and second solenoids, respectively. Let $\overline{O_1B} = \overline{O_2C} = r$ and ℓ represents the length of the pendulum. Since the magnet is fixed on the rod, its angular velocity is equal to the angular velocity of the pendulum.

2.2 Mathematical modeling

In this study, to simplify our analysis, the neodymium magnet and the solenoids are considered to be point magnets. The magnetic forces \vec{F}_1 and \vec{F}_2 produced, respectively, by the first and second solenoids on the neodymium magnet have the following forms [25]

$$\vec{F}_1 = \frac{\mu_0 Q_1 Q}{4\pi} \frac{\overrightarrow{BM}}{\|\overrightarrow{BM}\|^3} = \frac{\mu_0 Q_1 Q}{4\pi} \frac{(\ell \sin \theta - (\ell + r) \sin \alpha) \vec{i} - (\ell \cos \theta - (\ell + r) \cos \alpha) \vec{j}}{(2\ell(\ell + r)(1 - \cos(\theta - \alpha)) + r^2)^{\frac{3}{2}}}, \quad (1)$$

$$\vec{F}_2 = \frac{\mu_0 Q_2 Q}{4\pi} \frac{\overrightarrow{CM}}{\|\overrightarrow{CM}\|^3} = \frac{\mu_0 Q_2 Q}{4\pi} \frac{(\ell \sin \theta + (\ell + r) \sin \alpha) \vec{i} - (\ell \cos \theta - (\ell + r) \cos \alpha) \vec{j}}{(2\ell(\ell + r)(1 - \cos(\theta + \alpha)) + r^2)^{\frac{3}{2}}}. \quad (2)$$

Here, μ_0 is the permeability of the vacuum, Q_1 , Q_2 and Q are the pole strengths of the solenoids and neodymium magnet, respectively. Since the magnetic fields provided by the solenoids are governed by the currents $i_1(t)$ and $i_2(t)$ flowing through the respective windings, the strengths Q_1 and Q_2 are respectively proportional to the currents $i_1(t)$ and $i_2(t)$. They can be recast to the following forms: $Q_1 = ki_1(t)$ and $Q_2 = ki_2(t)$, where k stands for a constant parameter. The magnetic torques provided by the above magnetic forces \vec{F}_1 and \vec{F}_2 follow

$$\Gamma_a = \frac{\mu_0 k i_1 Q}{4\pi} \frac{\ell(\ell + r) \sin(\theta - \alpha)}{(2\ell(\ell + r)(1 - \cos(\theta - \alpha)) + r^2)^{\frac{3}{2}}}, \quad (3)$$

$$\Gamma_b = \frac{\mu_0 k i_2 Q}{4\pi} \frac{\ell(\ell + r) \sin(\theta + \alpha)}{(2\ell(\ell + r)(1 - \cos(\theta + \alpha)) + r^2)^{\frac{3}{2}}}. \quad (4)$$

After some algebraic transformations, the final magnetic torques take the following final form

$$\Gamma_1 = \frac{\sigma i_1 \sin(\theta - \alpha)}{(1 + \varepsilon - \cos(\theta - \alpha))^{\frac{3}{2}}} + \frac{\sigma i_2 \sin(\theta + \alpha)}{(1 + \varepsilon - \cos(\theta + \alpha))^{\frac{3}{2}}}, \quad (5)$$

$$\text{where } \sigma = \frac{k\mu_0 Q}{8\pi\sqrt{2\ell(\ell + r)}} \text{ and } \varepsilon = \frac{r^2}{2\ell(\ell + r)}.$$

Since the currents i_1 and i_2 are provided by current sources, the effects of the induced electromotive forces attributed to the movement of the neodymium magnet in the

solenoids are neglected. The application of Newton's second law to the pendulum yields the following equation of motion

$$J\ddot{\theta} + \beta\dot{\theta} + C\theta + mg\ell_1 \sin\theta + \Gamma_s(\dot{\theta}) = \Gamma_1. \quad (6)$$

Terms J and m are the pendulum moment of inertia and mass of the pendulum with the fixed magnet, respectively. Term ℓ_1 represents the distance from the pivot to the center of mass of the magnetic pendulum, β is a complete viscous damping coefficient, C is the stiffness of the joint and the parameter g stands for the gravitational acceleration. Finally, $\Gamma_s(\dot{\theta})$ represents the nonlinear part of the Stribeck friction torque and is defined as [26,28]

$$\Gamma_s(\dot{\theta}) = \left[M_c + (M_s - M_c) \exp\left(-\frac{\dot{\theta}^2}{v_s^2}\right) \right] \tanh(\chi\dot{\theta}). \quad (7)$$

In the above equation, M_c represents the magnitude of Coulomb friction, while M_s is the static friction value. The parameter v_s stands for Stribeck velocity, while χ is a regularization parameter [26,28].

Based on the experimental measurements carried out by the authors of reference [28], the system can also be described by the following second-order differential equation:

$$J\ddot{\theta} + \beta\dot{\theta} + C\theta + mg\ell_1 \sin\theta + \Gamma_s(\dot{\theta}) = \Gamma_2, \quad (8)$$

where Γ_2 is the torque exerted by the coils on the neodymium magnet. As defined in equation (5), Γ_2 is a function of the coil currents i_1 and i_2 and is related to the mechanical displacement θ :

$$\Gamma_2 = \frac{2i_1 a (\theta - \alpha)}{b} \exp\left(-\frac{(\theta - \alpha)^2}{b}\right) + \frac{2i_2 a (\theta + \alpha)}{b} \exp\left(-\frac{(\theta + \alpha)^2}{b}\right). \quad (9)$$

The fitting parameters a and b are also functions of the amplitudes of the currents through the coil. In what follows, we will assume that there are constants. The parameters used in this work follow the experimental results presented in reference [28] and are given in Table 1.

Parameters	Values	Parameters	Values
a	$4.253 \cdot 10^{-2}$ Nm rad	b	$1.818 \cdot 10^{-2}$ rad ²
r	0.100 m	ℓ	1.200 m
J	$6.787 \cdot 10^{-4}$ kgm ²	$\gamma = mg\ell_1$	$5.800 \cdot 10^{-2}$ Nm
β	$2.019 \cdot 10^{-4}$ Nm/rad	C	$1.742 \cdot 10^{-2}$ Nm/rad
M_c	$2.223 \cdot 10^{-4}$ Nm	M_s	$4.436 \cdot 10^{-4}$ Nm
v_s	$5.374 \cdot 10^{-1}$ rad/s	χ	5.759
f	$0.2 \text{ Hz} \leq f \leq 10.0 \text{ Hz}$	I_{m1}, I_{m2}	$0.0 \text{ A} \leq I_{m1} = I_{m2} \leq 5 \text{ A}$
I_1, I_2	$0.0 \text{ A} \leq I_1 = I_2 \leq 5 \text{ A}$		

Table 1 Values of the parameters used in this work [28].

3 States of the system powered by constant currents

3.1 Equilibrium points

Firstly, we determined and analyzed the structure of the equilibrium points of the system. In this regard, the system is not subjected to variable excitation, and therefore, the variable current sources i_1 and i_2 are replaced by constant current sources I_1 and I_2 , respectively. With constant current sources, a solution to equation (6) is expected to approach an equilibrium point. Setting the derivatives to zero in equation (6) yields

$$\frac{\sigma I_1 \sin(\theta - \alpha)}{(1 + \varepsilon - \cos(\theta - \alpha))^{\frac{3}{2}}} + \frac{\sigma I_2 \sin(\theta + \alpha)}{(1 + \varepsilon - \cos(\theta + \alpha))^{\frac{3}{2}}} - C\theta - \gamma \sin \theta = 0. \quad (10)$$

After some algebra manipulations, the approximated solutions of equation (10) are roots of the following polynomial

$$(D_1 + E_1\theta) \prod_{n=1}^2 \left[A_{1n} + 2B_{1n}(\theta + (-1)^n \alpha)^2 + C_{1n}(\theta + (-1)^n \alpha)^4 \right] = 0, \quad (11)$$

where

$$\begin{aligned} D_1 &= \sigma(I_1 - I_2)(1 + \varepsilon - \cos \alpha) \sin \alpha, \\ E_1 &= \frac{\sigma}{2} \left(3 - 2 \cos \alpha - 2\varepsilon \cos \alpha - \cos^2 \alpha \right) (I_1 + I_2) + (C + \gamma)(1 + \varepsilon - \cos \alpha)^{\frac{5}{2}}, \\ A_{1n} &= 480 \left(C\varepsilon^2 \cos \alpha + \gamma\varepsilon^2 - 2\sigma I_n \sqrt{\varepsilon} \cos \alpha \right), \\ B_{1n} &= 20 \left(9C\varepsilon \cos \alpha + 9\gamma\varepsilon - 2\gamma\varepsilon^2 + 4\sigma I_n \sqrt{\varepsilon} \cos \alpha \right), \\ C_{1n} &= 45C \cos \alpha - 30C\varepsilon \cos \alpha - 90\gamma\varepsilon + 45\gamma + 4\gamma\varepsilon^2 - 8\sigma I_n \sqrt{\varepsilon} \cos \alpha. \end{aligned} \quad (12)$$

Coefficients D_1 and E_1 are the coefficients of the first order series expansion of equation (10) around $\theta = 0$ rad. Similarly, the coefficients A_{1n} , $2B_{1n}$ and C_{1n} with $n = 1, 2$ are obtained by finding the fourth order series expansion of equation (10) around the points $\theta = \alpha$ and $\theta = -\alpha$, respectively. It is found that the possible real roots of equation (11) have the following forms:

$$\begin{aligned} \theta_a &= -\alpha - \sqrt{\frac{-B_{12} + \sqrt{B_{12}^2 - A_{12}C_{12}}}{C_{12}}}, \quad \theta_b = -\alpha, \quad \theta_o = -\frac{D_1}{E_1}, \quad \theta_c = \alpha \text{ and} \\ \theta_d &= \alpha + \sqrt{\frac{-B_{11} + \sqrt{B_{11}^2 - A_{11}C_{11}}}{C_{11}}}, \end{aligned} \quad (13)$$

To carry out the analysis in a general way, we consider that the currents I_1 and I_2 can independently have positive and negative values. Assuming the positive values of Q , the number of equilibrium points is defined through the signs of the applied currents I_1 and I_2 , and four important cases are obtained. Figure 2 compares the approximate solutions (13) to the ones obtained using the Newton-Raphson method to solve the equation (10) considering I_2 as the control parameter after fixing I_1 .

- (i) $I_1 \leq 0$ and $I_2 \leq 0$; there are three equilibrium points of the system, namely θ_b , θ_o and θ_c . This situation is illustrated in Figure 2a where the roots of equation (10) are plotted in black using the Newton-Raphson algorithm and for $I_1 = -1.0$ A.

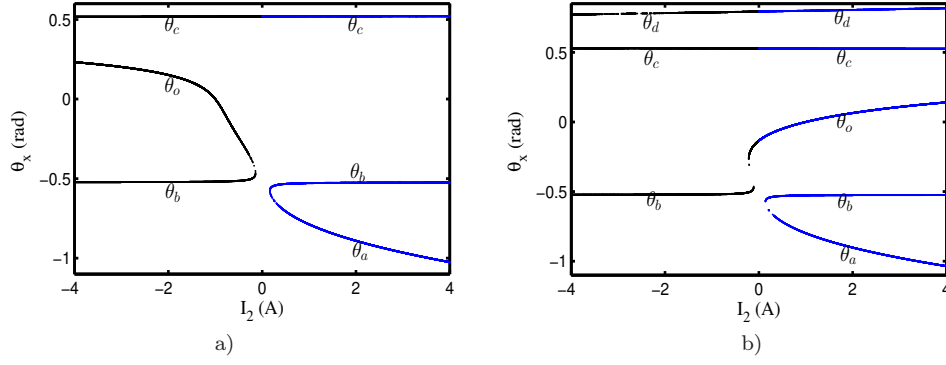


Fig. 2 Location of the equilibrium points obtained for $\alpha = \frac{\pi}{6}$ rad, and a) for $I_1 = -1.0$ A, while b) for $I_1 = 1.0$ A.

- (ii) $I_1 \leq 0$ and $I_2 > 0$; also three equilibrium points are obtained here. There are θ_a , θ_b and θ_c as shown in the graph of Figure 2a with the curves plotted in blue and for $I_1 = -1.0$ A.
- (iii) $I_1 > 0$ and $I_2 \leq 0$; the model still presents three equilibrium points given as θ_b , θ_c and θ_d . For verification, the roots of equations (11) are plotted with black in Figure 2b for $I_1 = 1.0$ A.
- (iv) $I_1 > 0$ and $I_2 > 0$; in this configuration, there are the following five equilibrium points: θ_a , θ_b , θ_o , θ_c and θ_d . This situation is highlighted with the curve in blue presented in Figure 2b where the roots of equations (10) are obtained using the Newton-Raphson algorithm for $I_1 = 1.0$ A.

Notably, Figure 2 presents excellent agreement between the approximate and numerical mathematical solutions.

3.2 Stability of the equilibrium points

According to the first, second, and third cases mentioned above, the first and third points are stable while the second point is unstable. The behavior is different in the last situation where the first, third, and fifth equilibrium points are stable while the second and the fourth are unstable. The stability of each equilibrium point θ_x is estimated based on the eigenvalues λ of the corresponding Jacobian matrix

$$M_J = \begin{bmatrix} 0 & 1 \\ \Gamma_e(\theta_x) - \frac{\beta + \chi M_s}{J} & \end{bmatrix}, \quad (14)$$

where

$$\Gamma_e(\theta) = \frac{\sigma i_1 \cos(2\theta - 2\alpha) + 4(1 + \varepsilon) \cos(\theta - \alpha) - 5}{4J [1 + \varepsilon - \cos(\theta - \alpha)]^{\frac{5}{2}}} + \frac{\sigma i_2 \cos(2\theta + 2\alpha) + 4(1 + \varepsilon) \cos(\theta + \alpha) - 5}{4J [1 + \varepsilon - \cos(\theta + \alpha)]^{\frac{5}{2}}} - \frac{C + mg l_1 \cos(\theta)}{J}. \quad (15)$$

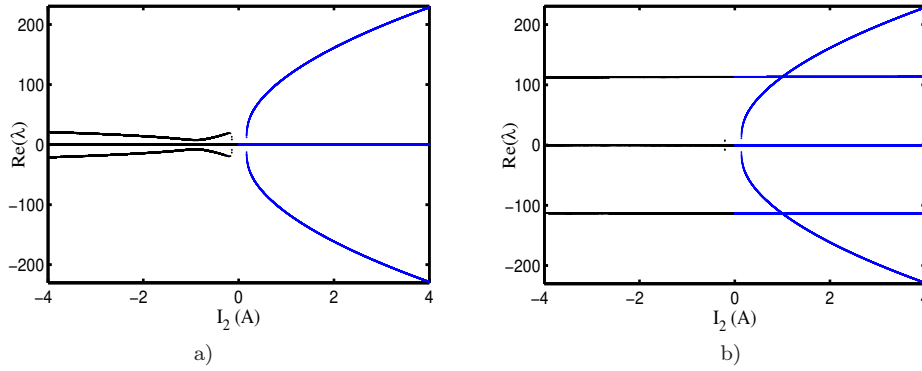


Fig. 3 Real parts of the eigenvalues of the corresponding Jacobian matrix obtained for $\alpha = \frac{\pi}{6}$ rad and a) for $I_1 = -1.5$ A, b) for $I_1 = 1.5$ A.

The real parts of the eigenvalues λ are reported in Figures 3a and 3b plotted for $I_1 = -1.0$ A and $I_1 = 1.0$ A, respectively.

The current I_2 is used as the control parameter and $\alpha = \frac{\pi}{6}$. Figure 3a shows two stable and one unstable equilibrium points. On the other hand, Figure 3b presents two stable and one unstable equilibrium points when I_2 is negative. For positive I_2 , there are three stable and two unstable equilibrium points. The black and blue colors imply the locations of the equilibrium points presented previously.

3.3 Shapes of the potential

The potential U associated with the differential equation (6) has the following form

$$U = \frac{2\sigma I_1}{\sqrt{1 + \varepsilon - \cos(\theta - \alpha)}} + \frac{2\sigma I_2}{\sqrt{1 + \varepsilon - \cos(\theta + \alpha)}} + \frac{1}{2}C\theta^2 - \gamma \cos \theta. \quad (16)$$

Different shapes of the potential are presented in Figure 4 for some configurations of the currents I_1 and I_2 . As demonstrated before in stability analysis of equilibrium points, Figure 4 presents globally three kinds of potential depending on the signs of the currents. The first one in Figure 4a corresponds to a bistable shape (two currents are equal and negative). The second form stands for the asymmetric bistable potential (currents have different signs). The orientation of the asymmetry depends on which current is negative or positive as can be seen in Figures 4b and 4c. The last tristable form is presented in Figure 4d, and it takes place when the two currents are positive and equal. Observed that the symmetric bistable shape from Figure 4a and symmetric tristable shape can be deformed to asymmetric bistable or asymmetric tristable shapes if the currents have the same signs, but are different.

Figure 5 presents the basin of attractions for the stationary solutions with regard to the initial conditions of the pendulum, i.e. its angular displacement and angular velocity. The red points and red crosses indicate the stable and unstable equilibrium points, respectively. Any initially condition inside the blue regions of Figures 5a, 5b, 5c) and 5d) will ultimately arrive at the stationary solution θ_b , θ_a , θ_b and θ_a , respectively. For initial conditions inside the cyan regions of Figures 5a, 5b, 5c) and 5d),

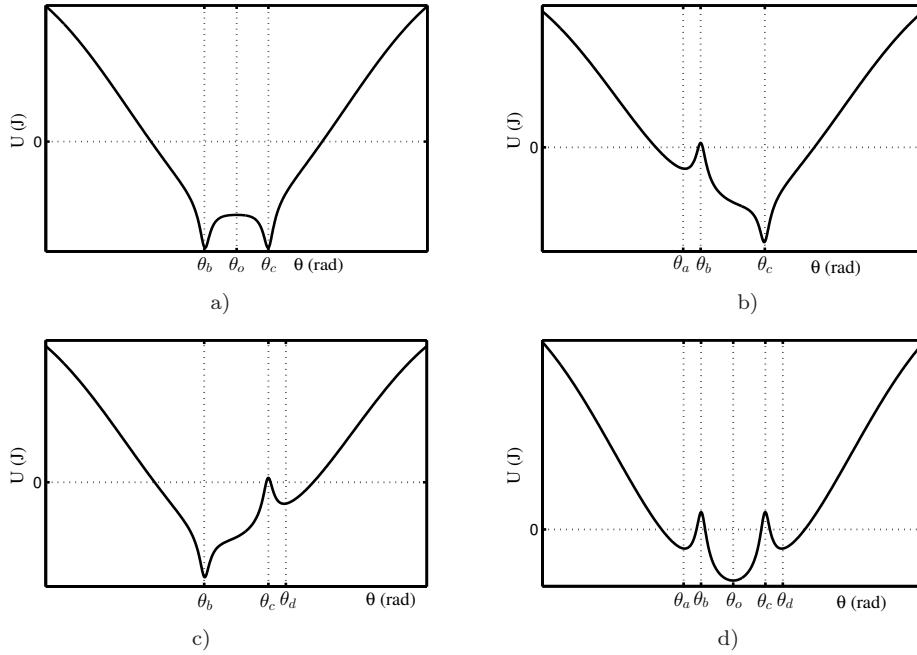


Fig. 4 Shape of the potential U for different values of the coil currents I_1, I_2 and for $\alpha = \frac{\pi}{6}$ rad. a) $I_1 = I_2 = -1.0$ A. b) $I_1 = -I_2 = -1.0$ A. c) $I_1 = -I_2 = 1.0$ A. d) $I_1 = I_2 = 1.0$ A.

the trajectories converge to the respective stable fixed point $\theta_c, \theta_b, \theta_d$ and θ_o . Finally, as shown in Figure 5d, for initial conditions that are inside the magenta region, the pendulum will be attracted by the equilibrium point θ_d .

One can notice that the basins of attractions of the system are dominant for initial values of θ and $\dot{\theta}$ in the vicinity of the equilibrium points. For large initial values of θ and $\dot{\theta}$, one can see a competition between the basin of attractions.

4 Dynamical states when the coil magnets are powered by AC currents.

We now analyze the situation where the coils are fed by sinusoidal current sources defined as $i_1 = I_{m1} \sin(\omega t)$ and $i_2 = I_{m2} \sin(\omega t - \varphi)$. Angular frequency $\omega = 2\pi f$, where f is the frequency, and φ represents the phase shift between the current sources. In this work, we will consider the case where the current sources are in phase ($\varphi = 0$ rad) and the case where they are out of phase ($\varphi = \pm\pi$ rad).

4.1 Bifurcation analysis

The richness of different dynamical behaviors exhibited by the system constituted of the magnetic pendulum and coils can be followed by the bifurcation diagrams. The investigated systems governed by the differential equation (6) have three control parameters $I_{m1} = I_{m2}$, f and α , and hence they are accessible experimentally, Figure 6

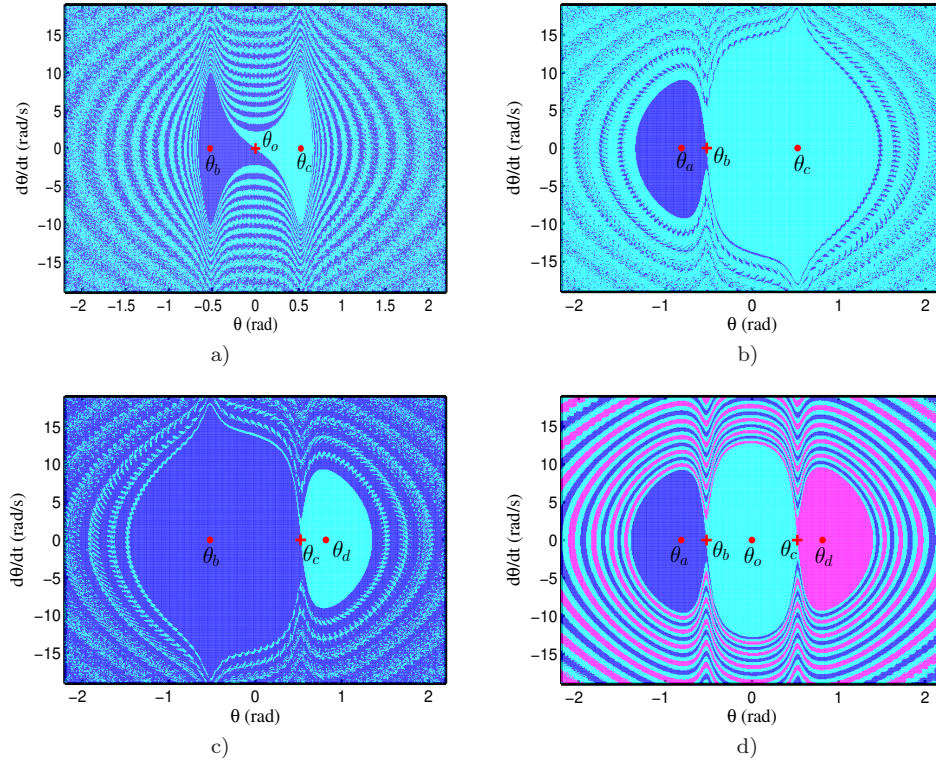


Fig. 5 Basins of attraction of the stationary solutions for different values of the currents I_1 and I_2 and for $\alpha = \frac{\pi}{6}$ rad: a) $I_1 = I_2 = -1.0$ A; b) $I_1 = -I_2 = -1.0$ A; c) $I_1 = -I_2 = 1.0$ A; d) $I_1 = I_2 = 1.0$ A.

shows the two-parameter bifurcation diagrams highlighting the two control parameters f and $I_{m1} = I_{m2}$ ($\alpha = \frac{\pi}{10}$ rad). Similarly, Figure 7 shows the two-parameter bifurcation diagrams where the dependence of the system on two control parameters f and $I_{m1} = I_{m2}$ ($\alpha = \frac{\pi}{6}$ rad) are employed.

Figures 6a and 7a are obtained when the current sources i_1 and i_2 are in phase ($\varphi = 0$ rad). On the other hand, Figures 6b and 7b are constructed when the current sources i_1 and i_2 are out of phase ($\varphi = \pi$ rad).

To identify the dynamical behavior of the system, the common way is to determine the number n in the period- n response when varying the control parameters. To each period- n response, with n , we have assigned a specific color. The white area denotes a region of no oscillation and the pendulum converges to one stable equilibrium point despite the time variation of the currents. Secondly, the black area, the magenta area, the red area, and the green area are attributed to the period-1, period-2, period-3, and period-4 trajectories, respectively. Thirdly, the cyan areas indicate a combination of period-5, period-6, period-7, period-8, period-9, and period-10. Finally, all responses with n greater than 10 and chaotic dynamics are marked by the blue area.

The bifurcation diagrams imply that the system does not perform oscillations for small amplitudes of the currents i_1 and i_2 being in phase. The region of no oscillation

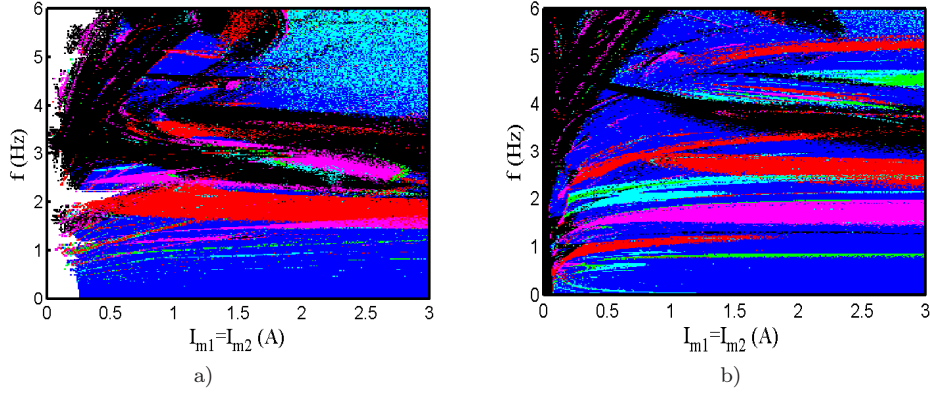


Fig. 6 Two-parameter bifurcation diagrams obtained when the current sources are a) in phase and b) out of phase in the plane $(I_{m1} = I_{m2}, f)$ and for $\alpha = \frac{\pi}{10}$ rad.

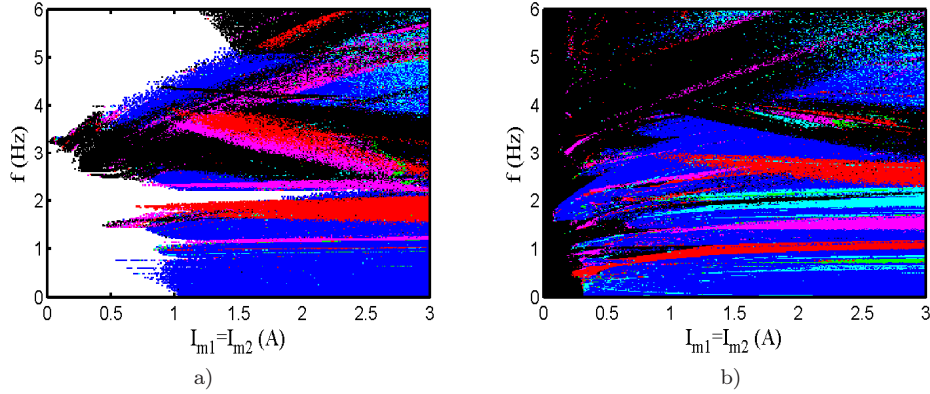


Fig. 7 Two-parameter bifurcation diagrams obtained when the current sources are a) in phase and b) out of phase in the plane $(I_{m1} = I_{m2}, f)$ and for $\alpha = \frac{\pi}{8}$ rad.

increases as the parameter α increases. When the currents i_1 and i_2 are out of phase, the pendulum performs period-1 oscillations for low current amplitudes. It should be emphasized that for frequencies above 4 Hz, the system becomes very sensitive to the variations of its parameters, in particular the frequency and the amplitudes of the currents delivered by the coils.

Furthermore, the effect of the frequency f on the angular displacement θ of the pendulum is shown in Figures 8a and 8b for $\varphi = 0$ rad and $\varphi = \pi$ rad, respectively, and fixed parameters $I_{m1} = I_{m2} = 1$ A and $\alpha = \frac{\pi}{10}$.

The bifurcation diagrams displayed in Figure 8a) and Figure 8b) are obtained by plotting local maxima of the angular displacement θ as a function of the frequency f of the external current sources, which increases in very small steps in the range $0 \text{ Hz} \leq f \leq 7 \text{ Hz}$. The corresponding Lyapunov exponents of Figure 8a) and Figure 8b) are plotted in Figure 8c) and Figure 8d) respectively. For the black curve, the initial

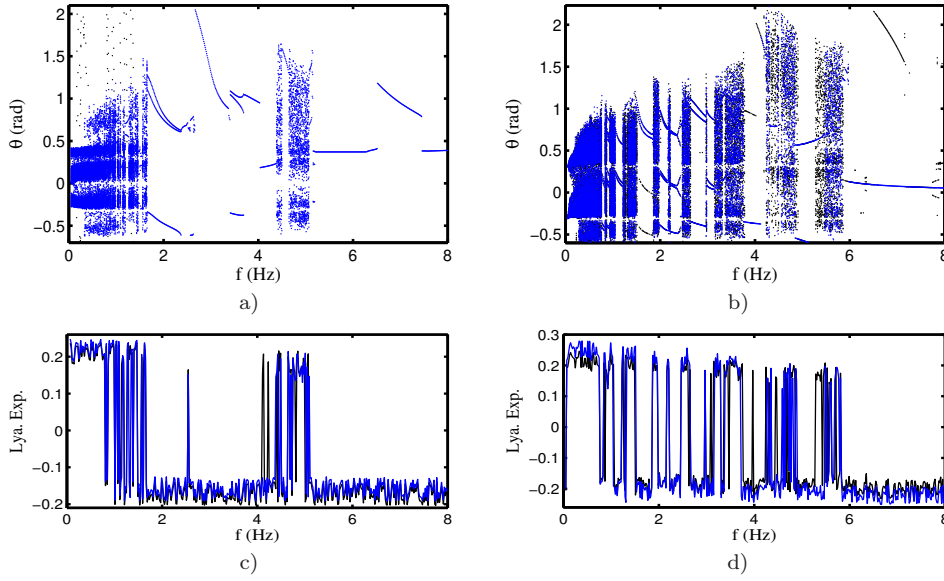


Fig. 8 Bifurcation diagrams and corresponding Lyapunov exponents as a function of the frequency f obtained for a) and c) in phase and b) and d) out-of-phase coil currents respectively. The black curve is obtained with the following initial condition: $\theta(0) = 0.57$ rad, $\dot{\theta}(0) = 5.0$ rad/s. The blue curve is obtained for increasing f , where the final state at each iteration is used as the initial state for the next iteration.

conditions at each iteration of the control parameter f are constant at $\theta(0) = -0.57$ rad, $\dot{\theta}(0) = 5.0$ rad/s. Meanwhile, for the blue curve, the final state at each iteration is used as the initial state for the next iteration. As the graphs reveal, good agreements are found between the bifurcation diagrams and the corresponding graphs of the Lyapunov exponents.

Based on the bifurcation diagrams presented in Figure 8, it might be noticed that the angular displacement θ of the pendulum displays different dynamical behaviors as the periodicities and the amplitudes of the variable θ are not the same. Hence, solutions to equation (6) exhibit multistability features in different intervals of the control parameter.

A confirmation of the multistable behavior of the system is presented in Figure 9 where one sees that for the same parameters different trajectories can be obtained depending on the values of the initial solutions. Figure 9a) presents a coexistence of four chaotic behaviors when the currents are in phase and $f = 1.35$ Hz. A similar behavior is presented in Figure 9b) plotted for $f = 1.35$ Hz and with the current sources out of phase, one sees a coexistence of four chaotic behaviors. The curves in black are obtained by using the initial conditions $\theta(0) = 0.57$ rad and $\dot{\theta}(0) = 8.14$ rad/s, the curves in blue are obtained by using the initial conditions $\theta(0) = 0.57$ rad, $\dot{\theta}(0) = -8.14$ rad/s, whereas the curves in magenta are obtained for the initial conditions $\theta(0) = -0.57$ rad, $\dot{\theta}(0) = -8.14$ rad/s. Finally, the curves in green are obtained with the following initial conditions $\theta(0) = -0.57$ rad and $\dot{\theta}(0) = 8.14$ rad/s.

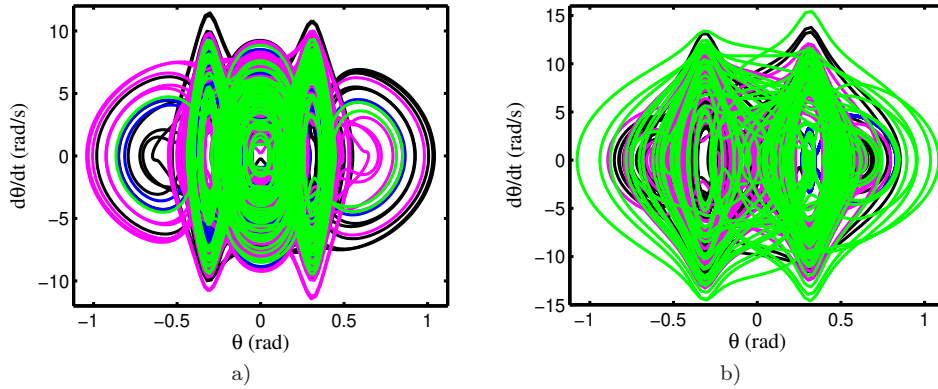


Fig. 9 Phase portraits illustrating the multistability of the system for parameters: $f = 1.35$ Hz, $\alpha = \frac{\pi}{10}$ rad and $I_{m1} = I_{m2} = 1.0$ A. Subfigure a) is obtained for in-phase ($\varphi = 0$ rad) coil currents, while b) corresponds to out of phase ($\varphi = \pi$ rad) coil currents. For both figures, the trajectories are computed for different initial conditions. The black curves ($\theta(0) = 0.57$ rad, $\dot{\theta}(0) = 8.14$ rad/s), blue curves ($\theta(0) = 0.57$ rad, $\dot{\theta}(0) = -8.14$ rad/s), magenta curves ($\theta(0) = -0.57$ rad, $\dot{\theta}(0) = -8.14$ rad/s), and green curves ($\theta(0) = -0.57$ rad, $\dot{\theta}(0) = 8.14$ rad/s).

4.2 Numerical and analytical analysis

Bifurcation diagrams shown in Figures 6a) and 7a), present domains/ranges of parameters where the system exhibits periodic solutions. For instance, in Figure 6a), period-1 oscillations exist for frequencies close to 3 Hz and for some range of current. In the same Figures 6a) and 7a), period-3 oscillations are present around the frequency 1.8 Hz or 2 Hz for current amplitude above 0.5 A (below this value, there is an alternation of different dynamical states). For Figures 6b) and 7b), period-1 oscillations for small values of the current amplitude (close to 0 mA) and for any frequency are observed. Therefore, numerical methods might be employed to determine the angular amplitude of oscillations and plot its amplitude versus the current amplitude or the frequency depending on the case considered. We have done this in the approximate form of the pendulum differential equation. We start with a situation where period-3 oscillations exist. Figure 10a) shows the phase portrait of the system for the following fixed parameters: $f = 1.8$ Hz, $I_{m1} = I_{m2} = 1$ A, $\varphi = 0$ rad and $\alpha = \frac{\pi}{10}$. The corresponding Fourier transform amplitude spectrum is presented in Figure 10b).

Namely, Figure 10b) shows that dominant frequency components are 0.9 Hz and 2.7 Hz, which correspond to $\frac{1}{2}f$ and $\frac{3}{2}f$, respectively. As shown in Figure 11, the situation is different if the currents i_1 and i_2 are out of phase. Figure 11 is obtained for $f = 2.0$ Hz, $I_{m1} = I_{m2} = 1$ A, $\varphi = \pi$ rad and $\alpha = \frac{\pi}{8}$ rad. As indicated in the corresponding frequency spectrum, the important frequency components are 0.66 Hz, 2.0 Hz, and 3.33 Hz. These frequencies are related to the frequency of the external sources, that is, $\frac{1}{3}f$, $\frac{3}{3}f$, and $\frac{5}{3}f$, respectively. For some sets of the system parameters, we found that the important frequency component is f , as illustrated in the graphs in Figure 12.

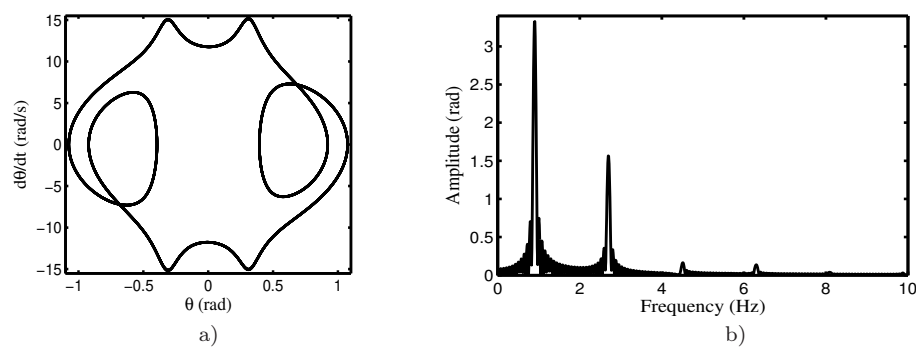


Fig. 10 a) Phase portrait of the system when $f = 1.8$ Hz, $I_{m1} = I_{m2} = 1$ A, $\varphi = 0$ rad and $\alpha = \frac{\pi}{10}$ rad. b) Corresponding frequency spectrum of angular displacement.

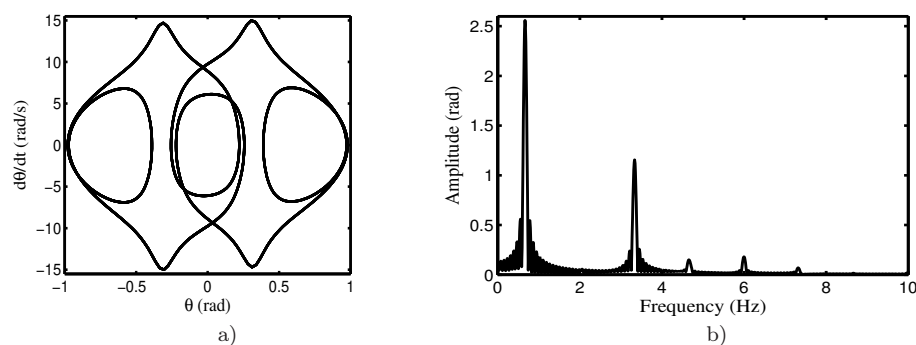


Fig. 11 a) Phase portrait of the system when $f = 2.0$ Hz, $I_{m1} = I_{m2} = 1$ A, $\varphi = \pi$ rad and $\alpha = \frac{\pi}{10}$ rad. b) Corresponding frequency spectrum of angular displacement.

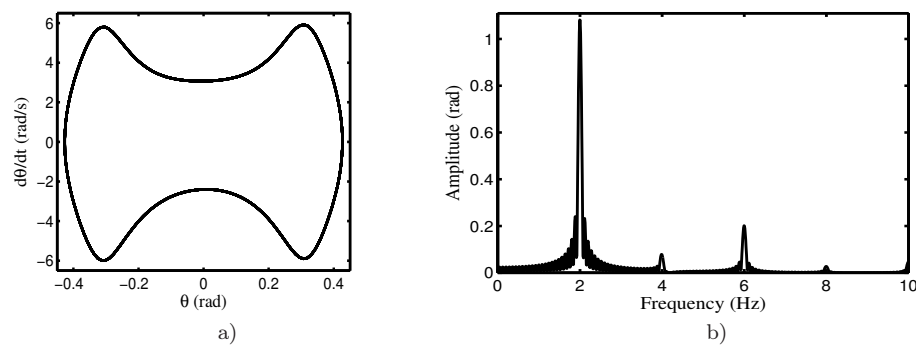


Fig. 12 a) Phase portrait of the system when $f = 2.0$ Hz, $I_{m1} = I_{m2} = 400$ mA, $\varphi = \pi$ rad and $\alpha = \frac{\pi}{10}$ rad. b) Corresponding frequency spectrum of angular displacement.

Figure 12 is plotted for $f = 2.0$ Hz, $I_{m1} = I_{m2} = 400$ mA, $\varphi = \pi$ rad and $\alpha = \frac{\pi}{10}$ rad. As indicated in the corresponding frequency spectrum, the crucial roles in the system dynamics are played by the frequency components f and $3f$.

In order to carry out analytical investigations, the differential equation (6) can be recast to the following form

$$J \frac{d^2\theta}{dt^2} + (\beta + \chi M_s) \frac{d\theta}{dt} + C\theta + \gamma \left(\theta - \frac{1}{6}\theta^3 \right) = \frac{\eta(\theta - \alpha)i_1}{(\theta - \alpha)^2 + \mu^2} + \frac{\eta(\theta + \alpha)i_2}{(\theta + \alpha)^2 + \mu^2}, \quad (17)$$

where Γ_s and $\sin\theta$ have been replaced by their corresponding first and third-order series expansions, respectively. The external torque has been approximated by ratios of polynomial functions, and the coefficient μ and η are defined as

$$\begin{aligned} \mu &= \pi - \arccos \left(1 + \varepsilon - \sqrt{\varepsilon^2 + 2\varepsilon + 4} \right), \\ \eta &= \frac{9\mu\sigma \sqrt{1 - (1 + \varepsilon - \sqrt{\varepsilon^2 + 2\varepsilon + 4})^2}}{(2\varepsilon + 2 - \sqrt{\varepsilon^2 + 2\varepsilon + 4})^{\frac{3}{2}}}. \end{aligned} \quad (18)$$

Owing to the value of the parameter φ , there are two different cases. In this section, we consider the situation where the currents i_1 and i_2 are in phase ($\varphi = 0$ rad). Taking advantage of the results obtained previously, and using the balanced harmonic method, we consider the solution of equation (17) in the form

$$\theta = A \cos \left(\frac{\omega t}{2} \right) + B \sin \left(\frac{\omega t}{2} \right). \quad (19)$$

At this level, the quantity $\theta_m = \sqrt{A^2 + B^2}$ is the amplitude of the analytical signal and represents our unknown variable. The substitution of equation (19) into the differential equation (17), and after some transformations, the amplitude θ_m is solution of the following twelfth order polynomial

$$A_{12}\theta_m^{12} + A_{10}\theta_m^{10} + A_8\theta_m^8 + A_6\theta_m^6 + A_4\theta_m^4 + A_2\theta_m^2 + A_0 = 0, \quad (20)$$

where

$$\begin{aligned} A_{12} &= 1225\gamma^2, \quad A_{10} = 5600\gamma(v\gamma + 3\psi), \\ A_8 &= 32 \left[72\beta'^2 + 5\gamma(61v^2 + 84\alpha^2v + 84\alpha^4) + 60\psi(41v\gamma + 30\psi) \right], \\ A_6 &= 256 \left[72v(\beta'^2 + 15\psi^2) + 30\gamma v(v + 2\alpha^2)^2 + 15\gamma^2\psi(37v^2 + 52v\alpha^2 + 52\alpha^4) \right], \\ A_4 &= 73728 \left[\beta'^2(v^2 + 2v\alpha^2 + 2\alpha^4) + \psi^2(7v^2 + 10v\alpha^2 + 10\alpha^4) \right] + \\ &\quad 256(v + 2\alpha^2)^2 \left[9\gamma^2(v + 2\alpha^2)^2 + 456\gamma\psi v \right], \\ A_2 &= 36864(v + 2\alpha^2)^2 \left[4v(\beta'^2 + 3\psi^2) + \gamma\psi(v + 2\alpha^2)^2 \right], \\ A_0 &= -v^2\eta^2 \left[(I_{m1} + I_{m2}\cos\varphi)^2 + I_{m2}^2\sin^2\varphi \right] + 4(\beta'^2 + \psi^2)(v + 2\alpha^2)^4. \end{aligned} \quad (21)$$

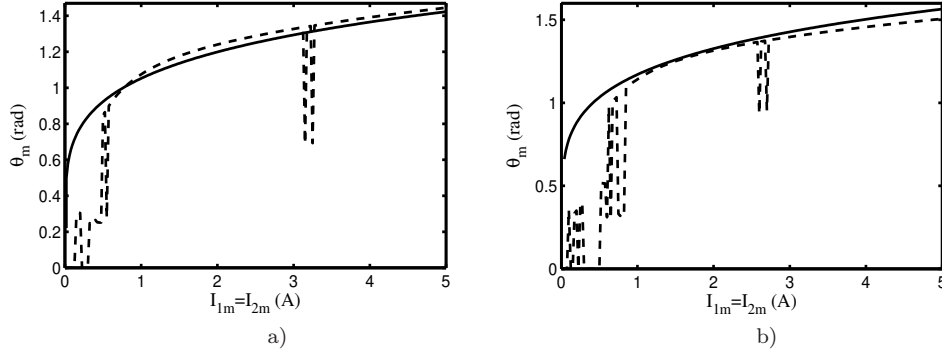


Fig. 13 Amplitude of angle θ_m versus the magnitudes $I_{m1} = I_{m2}$ of the current sources for $f = 1.8$ Hz and $\varphi = 0$ rad. a) $\alpha = \frac{\pi}{10}$ rad and b) $\alpha = \frac{\pi}{8}$ rad. The curves with solid lines correspond to analytical results, while the curves with dashed lines are obtained numerically.

The newly introduced parameters $\beta' = (\beta + \chi M_s)\omega$, $v = \mu^2 - \alpha^2$ and $\psi = J\omega^2 - C - \gamma$ are used to simplify the notations. In the latter case, the opposite current sources do not affect the amplitude of the pendulum.

To verify our analysis, we use the magnitudes $I_{m1} = I_{m2}$ of the current sources as the control parameter, and the system is analyzed for two different angles α . Figure 13a) and Figure 13b) are plotted for $\alpha = \frac{\pi}{10}$ rad and $\alpha = \frac{\pi}{8}$ rad, respectively. The frequency used in Figure 13 is $f = 1.8$ Hz and the currents are in phase.

The analytical/numerical solutions are plotted with solid/dashed lines. Figures 13a) and 13b) indicate excellent agreement between our analytical and simulation results when the current amplitudes are greater than 0.5 A and 0.8 A, respectively. This can be understood since as presented in Figure 6, the responses of the system are dominated by period-3 oscillations. Equation (19) implies that $\frac{1}{2}f$ is the important frequency component of the response signal. In the other regions of Figures 13a) and 13b) ($I_m < 0.5$ A and $I_m < 0.8$ A), the alternation of different dynamical states including chaotic oscillations is observed. This is illustrated in the phase portraits of Figure 14a) and Figure 15a) plotted for $\varphi = \frac{\pi}{10}$ rad and $\varphi = \frac{\pi}{8}$ rad respectively.

Figures 14a) and 15a) are obtained for $f = 1.8$ Hz and $I_{m1} = I_{m2} = 200$ mA. As indicated in the corresponding frequency spectrum presented in Figures 14b) and 15b), the important frequency components are 0.0 Hz, 1.8 Hz, 2.7 Hz, and 3.6 Hz. These frequencies are related to the frequency of the external sources as $\frac{0}{2}f$, $\frac{2}{2}f$, $\frac{3}{2}f$, and $\frac{4}{2}f$, respectively. Consequently, the approximated analytical solution for $I_m < 0.5$ A and $I_m < 0.8$ A will have the following form

$$\theta = \theta_0 + A_1 \cos(\omega t) + B_1 \sin(\omega t). \quad (22)$$

It should be noticed that for certain small values of the current magnitudes, and hence the pendulum comes to rest after the transient process.

Similar analysis can be performed when the currents i_1 and i_2 are out of phase. But one has to notice that the important frequency component is generally $\frac{1}{2}f$ when the current sources are in phase. In contrast, when the current sources are out of phase, the significant frequency component is $\frac{1}{3}f$ and sometimes $\frac{3}{3}f$.

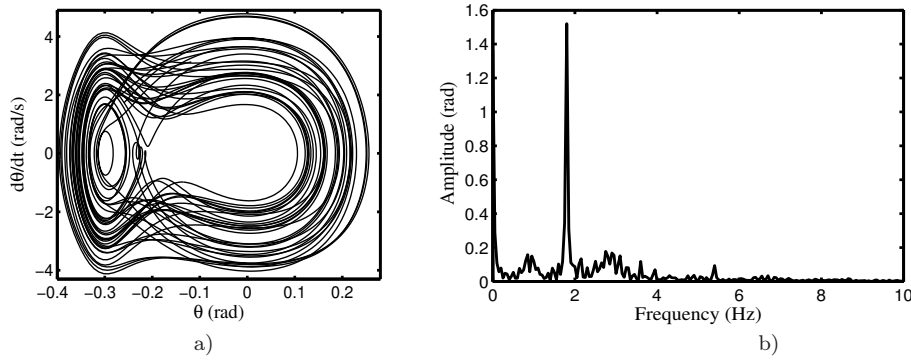


Fig. 14 Bifurcation diagrams as a function of the amplitude $I_{m1} = I_{m2}$ and plotted for different values of α : a) $\alpha = \frac{\pi}{10}$ rad and b) $\alpha = \frac{\pi}{8}$ rad.

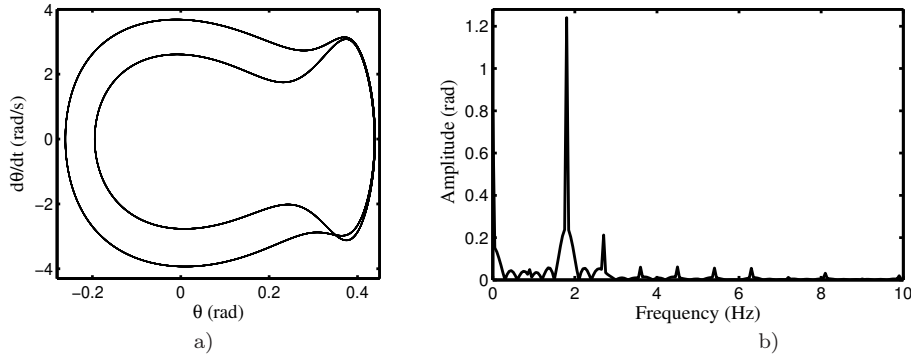


Fig. 15 Bifurcation diagrams as a function of the amplitude $I_{m1} = I_{m2}$ and plotted for different values of α : a) $\alpha = \frac{\pi}{10}$ rad and b) $\alpha = \frac{\pi}{8}$ rad.

5 Laboratory

5.1 Experimental rig

The experimental rig is presented in Figure 16a) and consists of a pendulum (1) with a neodymium magnet (2) attached at the tip. Electric coils (3) are placed symmetrically on both sides of the resting pendulum at an angle of 30 degrees.

The pendulum is suspended on a brass shaft (4) supported by ball bearings. The angular position measurement is performed using an incremental optical encoder (5). All construction is made of non-magnetic materials like textile composites, aluminum, brass, and polymer materials. Thanks to that the magnet-coils interaction is protected from external undesired magnetic effects like induction of eddy currents or additional magnetic fields of some ferromagnetic parts.

The electric coils characterized by 22 mH of inductance and 10.6 Ω of resistance are powered by two electronic systems based on OPA541AP operational amplifiers. The signal flow diagram in the system is shown in Figure 16b). The task of the electronic

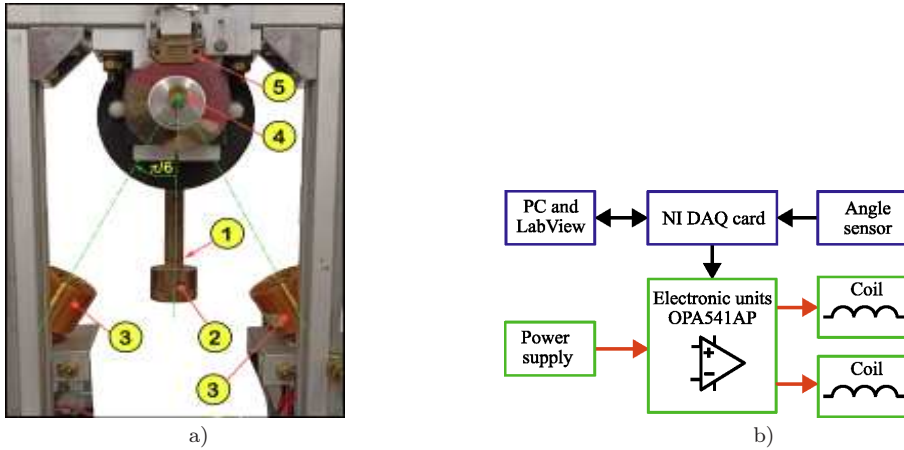


Fig. 16 Experimental setup of magnetic pendulum subjected to two electric coils (a), where: 1-pendulum, 2-neodymium magnet, 3-electric coil, 4-brass shaft, 5-incremental optical encoder.

systems is to convert the voltage signal coming from the NI DAQ card into a current signal flowing in the coils. The voltage signal is generated in the LabView program, which is also responsible for displaying the information collected by the HEDS-6140-B13 angle position sensor. The source of electricity powering the coils is the KORAD 3305D power supply. Due to the maximum current and voltage efficiency (30V 5A for two channels), we were not able to obtain experimentally all the numerical results contained in this paper.

5.2 Experimental vs. numerical results

By varying the frequency and amplitudes of the current sources while keeping the angle α constant at $\alpha = \frac{\pi}{6}$ rad, the simulation results using the two models described earlier are compared to the experimental ones.

We first consider the case where the current sources are in phase ($\varphi = 0$ rad) and the results are presented in Figures 17, 18 and 19. Figures 17a), 18a) and 19a) show the simulation results obtained from the first model, while Figures 17c), 18c) and 19c) are attributed to simulation results of the second model. For comparison, the experimental results are given in Figures 17b), 18b) and 19b).

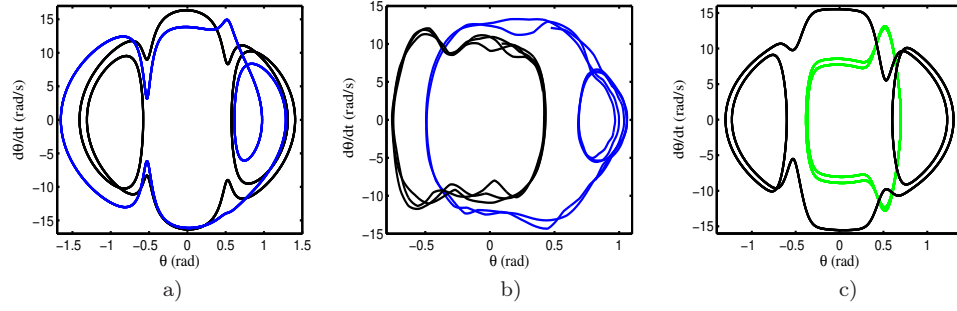


Fig. 17 Different phase portraits of the system. a) Obtained numerically using the first model (6), b) obtained experimentally, and c) obtained numerically using the second model (8), for: $I_{m1} = I_{m2} = 1.5$ A, $f = 3.5$ Hz, $\alpha = \frac{\pi}{6}$ rad and $\varphi = 0$ rad. Black curves are plotted for: $\theta(0) = 0.57$ rad, $\dot{\theta}(0) = 8.14$ rad/s. Blue and green curves are plotted for: $\theta(0) = 0.0$ rad, $\dot{\theta}(0) = 0.14$ rad/s and $\theta(0) = 0.232$ rad, $\dot{\theta}(0) = -9.968$ rad/s, respectively.

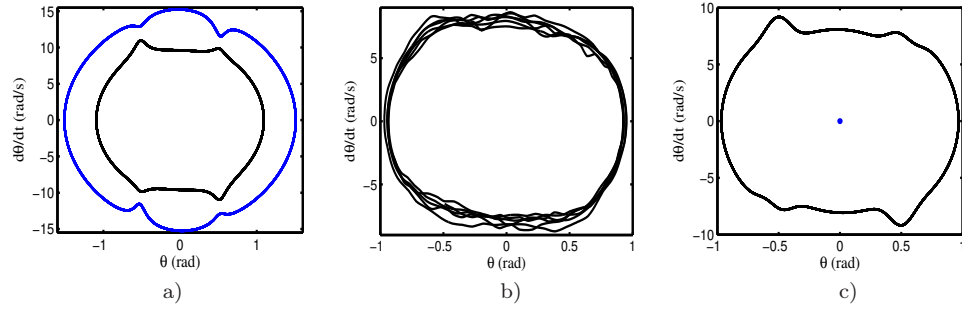


Fig. 18 Different phase portraits of the system. a) Obtained numerically using the first model (6), b) obtained experimentally, and c) obtained numerically using the second model (8), for: $I_{m1} = I_{m2} = 500$ mA, $f = 3.0$ Hz, $\alpha = \frac{\pi}{6}$ rad and $\varphi = 0$ rad. Black curves are plotted for: $\theta(0) = 0.57$ rad, $\dot{\theta}(0) = 8.14$ rad/s. Blue and green curves are plotted for: $\theta(0) = 0.0$ rad, $\dot{\theta}(0) = 0.14$ rad/s and $\theta(0) = 0.232$ rad, $\dot{\theta}(0) = -9.968$ rad/s, respectively.

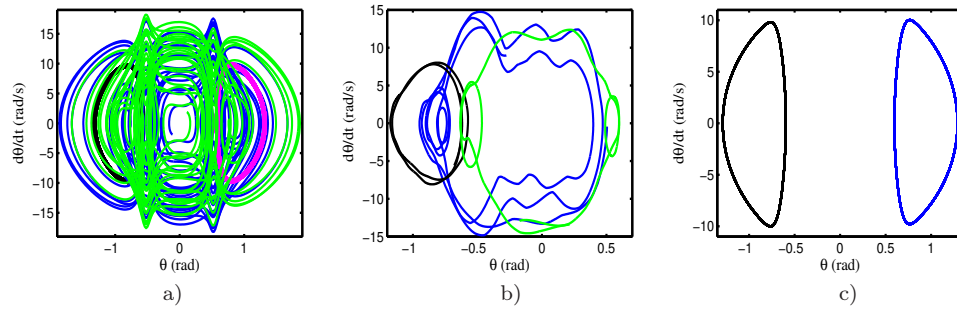


Fig. 19 Different phase portraits of the system. a) Obtained numerically using the first model (6), b) obtained experimentally, and c) obtained numerically using the second model (8), for: $I_{m1} = I_{m2} = 1.5$ A, $f = 4.0$ Hz, $\alpha = \frac{\pi}{6}$ rad and $\varphi = 0$ rad. Black and blue curves are plotted for: $\theta(0) = 0.57$ rad, $\dot{\theta}(0) = 8.14$ rad/s and $\theta(0) = 0.57$ rad, $\dot{\theta}(0) = -8.14$ rad/s, respectively. Magenta and green curves are plotted for: $\theta(0) = -0.57$ rad, $\dot{\theta}(0) = -8.14$ rad/s and $\theta(0) = -0.57$ rad, $\dot{\theta}(0) = 8.14$ rad/s, respectively.

As one can notice from the graphs, the multistable behavior observed theoretically is confirmed by the experimental results.

We aim now to visualize the dynamical behavior of the system when the current sources are out of phase $\varphi = \pi$ rad. As we have proceeded above, our results are presented in Figures 20 and 21. Figures 20a) and 21a) show the simulation results obtained from the first model while Figures 20c) and 21c) are simulation results obtained using the second model. For comparison, the experimental results are presented in Figures 20b) and 21b).

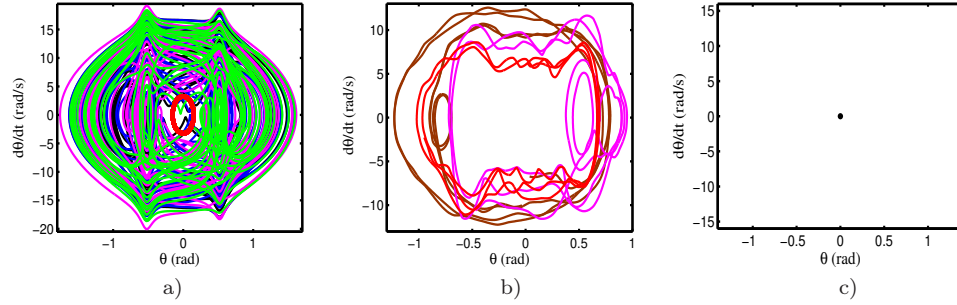


Fig. 20 Different phase portraits of the system. a) Obtained numerically using the first model (6), b) obtained experimentally, and c) obtained numerically using the second model (8), for: $I_{m1} = I_{m2} = 1$ A, $f = 3.5$ Hz, $\alpha = \frac{\pi}{6}$ rad and $\varphi = \pi$ rad. Black and blue curves are plotted for: $\theta(0) = 0.57$ rad, $\dot{\theta}(0) = 8.14$ rad/s and $\theta(0) = 0.57$ rad, $\dot{\theta}(0) = -8.14$ rad/s, respectively. Magenta and green curves are plotted for: $\theta(0) = -0.57$ rad, $\dot{\theta}(0) = -8.14$ rad/s and $\theta(0) = -0.57$ rad, $\dot{\theta}(0) = 8.14$ rad/s, respectively. Finally, red curve is plotted for: $\theta(0) = 0.0$ rad, $\dot{\theta}(0) = 5.0$ rad/s.

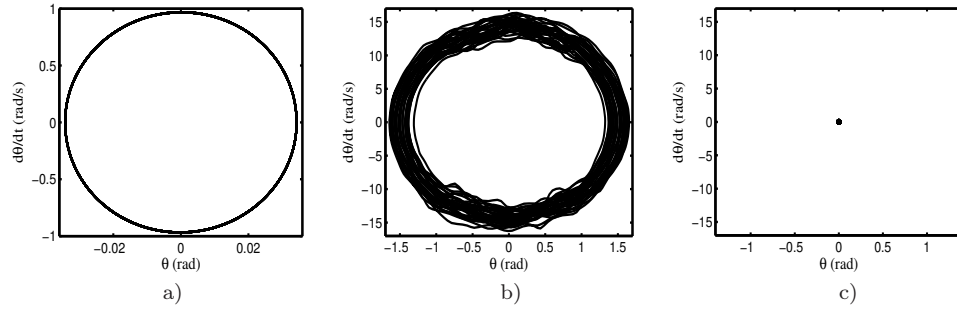


Fig. 21 Different phase portraits of the system. a) Obtained numerically using the first model (6), b) obtained experimentally, and c) obtained numerically using the second model (8), for: $I_{m1} = I_{m2} = 500$ mA, $f = 4.5$ Hz, $\alpha = \frac{\pi}{6}$ rad and $\varphi = \pi$ rad. The initial conditions for the numerical simulations are $\theta(0) = 1.6$ rad, $\dot{\theta}(0) = 5.5$ rad/s .

6 Concluding remarks

We have analyzed the dynamical states of a magnetic pendulum commanded by two coil magnets disposed symmetrically to the vertical stable position. First considering the coil is powered by constant current, we showed that the system presents different shapes for the potential corresponding to bistable and tristable dynamic states, both of which can be symmetric or asymmetric depending on the sign of the currents and their values. When the currents are sinusoidal functions, two-dimensional bifurcation diagrams (with the frequency and amplitudes of the current as the bifurcation parameters) have been plotted resulting in the system being able to exhibit several dynamical states such as period- n oscillations, chaos, and domains where there is no oscillation although the current is time-dependent. Plotting the variety of bifurcation diagrams versus the frequency under different initial conditions, it appears that the system can also present multistability with the coexistence of period-1T oscillations and chaos for the same set of parameters. The effects of the value of the separation angle between the coil magnets as well as that of the current being in phase or out of phase have also been analyzed. In the region where the oscillations are of period-2, we have employed the harmonic balance method. It has been found that the analytical amplitudes of oscillations have been confirmed by the numerical simulation.

The theoretical part of our paper has been complemented by the experimental investigation. However, one should note that the system is very sensitive to initial conditions leading to multistability so that the correspondence between the theoretical and experimental results is obtained only for specially selected initial conditions.

The results presented in this paper can be used to develop or optimize devices based on magnetic pendulums and aimed at energy recovery. As indicated by earlier works [38] in such systems the most energy can be stored in the chaotic regime, therefore further work will be based on the problem of chaos control and destabilization of periodic orbits in magnetic pendulum systems.

Acknowledgements The work of the second author K. Polczyński (experiment, numerical calculations, signal processing, and writing) and the last author J. Awrejcewicz (writing, editing, founding) was supported by the National Science Center, Poland under the grant OPUS 26 No. 2023/51/B/ST8/00021.

References

1. M. Hasan, P. Deepu, K. Kumar, A. Agrawal, D. Meena, Oscillation decay of a pendulum by an air jet, *Physics Letters A* 481 (2023) 129003.
2. S. Skurativskiy, K. Polczyński, M. Wojna, J. Awrejcewicz, Quantifying periodic, multi-periodic, hidden and unstable regimes of a magnetic pendulum via semi-analytical, numerical and experimental methods, *Journal of Sound and Vibration* 524 (2022) 116710.
3. A. Siuka, M. Schöberl, Applications of energy based control methods for the inverted pendulum on a cart, *Robot. Auton. Syst.* 57 (2009) 1012–1017.
4. W. Chu, Y. Wang, Vibration control of a flexible inverted pendulum using the planned flywheel motion, *Journal of Sound and Vibration* (2011) 117975.
5. J. Yue, Z. Zhou, J. Jiang, Y. Liu, D. Hu, Balancing a simulated inverted pendulum through motor imagery: an eeg-based real-time control paradigm, *Neurosci. Lett.* 524 (2012) 95–100.
6. K. Al-Solihat, M. Al Janaideh, Dynamic modeling and nonlinear oscillations of a rotating pendulum with a spinning tip mass, *Journal of Sound and Vibration* 548 (2023) 117485.
7. L. Franca, M. Savi, Distinguishing periodic and chaotic time series obtained from an experimental nonlinear pendulum, *Nonlinear Dynamics* 3 (2001) 255–273.

8. A. de Paula, M. Savi, F. Pereira-Pinto, Chaos and transient chaos in an experimental nonlinear pendulum, *J. Sound Vib* 3 (2006) 585–595.
9. W. Bessa, A. de Paula, M. Savi, Chaos control using an adaptive fuzzy sliding mode controller with application to a nonlinear pendulum, *Chaos Solitons Fractals* 2 (2009) 784–791.
10. A. A. Burov, A. D. Guerman, I. I. Kosenko, V. I. Nikonov, Dynamics of a pendulum anchored to a rotating asteroid, *IFAC-PapersOnLine* 51 (2) (2018) 867–872.
11. P. Zhao, Q. Quan, S. Chen, D. Tang, Z. Deng, Experimental investigation on hover performance of a single-rotor system for mars helicopter, *Aerospace Science and Technology* 86 (2019) 582–591.
12. M. Eshaghi, M. Ghasemi, K. Khorshidi, Design, manufacturing and applications of small-scale magnetic soft robots, *Extreme Mechanics Letters* 44 (2021) 101268.
13. H. Jaafar, Z. Mohamed, M. Ahmad, N. Wahab, L. Ramli, M. Shaheed, Control of an underactuated double-pendulum overhead crane using improved model reference command shaping: Design, simulation and experiment, *Mechanical Systems and Signal Processing* 151 (2021) 107358.
14. I. Izadgoshasb, Y. Y. Lim, L. Tang, R. V. Padilla, Z. S. Tang, M. Sedighi, Improving efficiency of piezoelectric based energy harvesting from human motions using double pendulum system, *Energy Conversion and Management* 184 (2019) 559–570.
15. X. Chen, L. Gao, J. Chen, S. Lu, H. Zhou, T. Wang, A. Wang, Z. Zhang, S. Guo, X. Mu, Z. L. Wang, Y. Yang, A chaotic pendulum triboelectric-electromagnetic hybridized nanogenerator for wave energy scavenging and self-powered wireless sensing system, *Nano Energy* 69 (2020) 104440.
16. K. King, S. Yoon, N. Perkins, K. Najafi, Wireless mems inertial sensor system for golf swing dynamics, *Sensors and Actuators A: Physical* 141 (2) (2008) 619–630.
17. I. P. Prikhodko, S. A. Zotov, A. A. Trusov, A. M. Shkel, Foucault pendulum on a chip: Rate integrating silicon mems gyroscope, *Sensors and Actuators A: Physical* 177 (2012) 67–78.
18. G. Khomeriki, Parametric resonance induced chaos in magnetic damped driven pendulum, *Physics Letters A* 380 (31) (2016) 2382–2385.
19. B. Nana, S. Yamgoué, R. Tchitnga, P. Wofo, Dynamics of a pendulum driven by a dc motor and magnetically controlled, *Chaos, Solitons and Fractals* 104 (2017) 18–27.
20. M. Wojna, A. Wijata, G. Wasilewski, J. Awrejcewicz, Numerical and experimental study of a double physical pendulum with magnetic interaction, *Journal of Sound and Vibration* 430 (2018) 214–230.
21. K. Witkowski, G. Kudra, S. Skurativskiy, G. Wasilewski, J. Awrejcewicz, Modeling and dynamics analysis of a forced two-degree-of-freedom mechanical oscillator with magnetic springs, *Mechanical Systems and Signal Processing* 148 (2021) 107138.
22. V. Puzyrov, J. Awrejcewicz, N. Losyeva, N. Savchenko, On the stability of the equilibrium of the double pendulum with follower force: Some new results, *Journal of Sound and Vibration* 523 (2022) 116699.
23. M. Shliomis, M. Zaks, Ferrofluidic torsional pendulum driven by oscillating magnetic field, *Phys. Rev. E* 73 (2006) 6–20.
24. T. Volkova, T. Zeidis, V. Naletova, K. Zimmermann, The dynamical behavior of a spherical pendulum in a ferrofluid volume influenced by a magnetic force, *Arch. Appl. Mech.* 86 (2016) 1591–1603.
25. B. Nana, S. Yamgoué, R. Tchitnga, P. Wofo, Nonlinear dynamics of a sinusoidally driven lever in repulsive magnetic fields, *Nonlinear Dynamics* 91 (2018) 55–66.
26. A. Siahmakoun, A. Valentina, J. Patterson, Nonlinear dynamics of a sinusoidally driven pendulum in a repulsive magnetic field, *American Journal of Physics* 65 (1997) 393–400.
27. G. Khomeriki, Parametric resonance induced chaos in magnetic damped driven pendulum, *Physics Letters A* 380 (2016) 2382–2385.
28. A. Wijata, K. Polczynski, J. Awrejcewicz, Theoretical and numerical analysis of regular one-side oscillations in a single pendulum system driven by a magnetic field, *Mechanical Systems and Signal Processing* 150 (2021) 1–22.
29. R. Fotsa, P. Wofo, Chaos in a new bistable rotating electromechanical system, *Chaos Solitons and Fractals* 93 (2016) 48–57.
30. S. Skurativskiy, K. Ploczynski, M. Wojna, J. Awrejcewicz, Quantifying periodic, multiperiodic, hidden and unstable regimes of a magnetic pendulum via semi-analytical, numerical and experimental methods, *Journal of Sound and Vibration* 254 (2022) 1–13.

31. Y. Kraftmakher, Experiments with a magnetically controlled pendulum, *European Journal of Physics* 28 (2007) 1007–1020.
32. P. Atzampou, P. C. Meijers, A. Tsouvalas, A. V. Metrikine, Contactless control of suspended loads for offshore installations: Proof of concept using magnetic interaction, *Journal of Sound and Vibration* 575 (2024) 118246.
33. V. N. Pilipchuk, K. Polczyński, M. Bednarek, J. Awrejcewicz, Guidance of the resonance energy flow in the mechanism of coupled magnetic pendulums, *Mechanism and Machine Theory* 176 (2022) 105019.
34. F. Fereidoony, S. P. M. Nagaraja, J. Paul, D. Santos, Y. E. Wang, Efficient ULF Transmission Utilizing Stacked Magnetic Pendulum Array, *IEEE Transactions on Antennas and Propagation* 70 (2022) 585–597.
35. M. N. Srinivas Prasad, F. Fereidoony, Y. E. Wang, 2D Stacked Magnetic Pendulum Arrays for Efficient ULF Transmission, in: 2020 IEEE International Symposium on Antennas and Propagation and North American Radio Science Meeting, IEEECONF 2020 - Proceedings, Institute of Electrical and Electronics Engineers Inc., Toronto, 2020, pp. 1305–1306.
36. B. Nana, K. Polczyński, P. Wofo, J. Awrejcewicz, Analysis of the nonlinear dynamics of a single pendulum driven by a magnetic field using the magnetic charges interaction model and the experimentally fitted interaction model, *Mechanical Systems and Signal Processing* 209 (2024) 111114.
37. D. Grzelczyk, M. Wojna, E. Ogińska, G. Wasilewski, J. Awrejcewicz, Numerical and experimental investigation of a magneto-electro-mechanical oscillator with a new magnet-coil interaction model and energy harvesting, *Journal of Sound and Vibration* 583 (2024) 118427.
38. R. Kumar, S. Gupta, S. F. Ali, Energy harvesting from chaos in base excited double pendulum, *Mechanical Systems and Signal Processing* 124 (2019) 49–64.

DECLARATIONS

Funding

The work of K. Polczyński and J. Awrejcewicz was supported by the National Science Center, Poland under the grant OPUS 26 No. 2023/51/B/ST8/00021.

Conflict of interest

The authors declare that they have no known competing financial interests or personal relationships that could have appeared to influence the work reported in this paper.

Availability of data and material

Not applicable

Code availability

Not applicable

Authors' contributions

Nana B.: Conceptualization, Methodology, Writing-Original draft preparation.; **Polczyński K.:** Writing-Reviewing and Editing. **Woaf P.:** General verification and Editing. **Awrejcewicz J.:** Supervision.

Ethics approval

Informed consent was obtained verbally before submission of this manuscript.

Consent to participate

We, Nana B., Polczyński K., Woaf P., and Awrejcewicz J. voluntarily agree to participate in this research study.

Consent for publication

We, Nana B., Polczyński K., Woaf P., and Awrejcewicz J. voluntarily agree to submit this research study for possible publication in this Journal (Nonlinear Dynamics).